Extreme Mechanics Letters 57 (2022) 101912

Contents lists available at ScienceDirect

Extreme Mechanics Letters

journal homepage: www.elsevier.com/locate/eml

Decoupling toughness and strength through architected plasticity

Sage Fulco [a], Michal K. Budzik [b,*], Erich D. Bain [c,1], Kevin T. Turner [a,*]

[a] Department of Mechanical Engineering and Applied Mechanics, University of Pennsylvania, Philadelphia, PA, 19104, USA
[b] Department of Mechanical Engineering and Production, Aarhus University, Aarhus, Denmark
[c] Weapons and Materials Research Directorate, US Army Research Lab, Aberdeen Proving Ground, MD, 21001, USA

ARTICLE INFO

Article history:
Received 30 June 2022
Received in revised form 30 September 2022
Accepted 18 October 2022
Available online 26 October 2022

Keywords:
Fracture toughness
Architecture
Interfaces
Plasticity

ABSTRACT

We investigate the elastic–plastic fracture of architected materials through experiments and theory, with a focus on understanding the combined effects of material length scale and geometry, using a pillar array as a model structure. We show that load sharing across the pillars, and hence toughness, can be controlled by changing the spatial distribution and height of the pillars. A simple relation is presented to relate the extent of the plastic fracture process zone to the pillar array structure and the resulting toughness. This relation allows for quantitative prediction of failure loads of specimens with plasticity localized to a structured region and reveals that strength and toughness can be decoupled through architecture. Our findings establish a foundation for design of architected materials with enhanced fracture toughness.

1. Introduction

Geometrically structured mechanical metamaterials have shown significant promise and have garnered much excitement for realizing materials with unprecedented properties. Architecture has been leveraged to create materials with high stiffness- and strength-to-weight ratios [1–4] and increased energy absorption [5–7]. However, geometry has not been widely exploited to engineer the fracture toughness of materials. To date, there are only a handful of works that employ geometric modifications to tailor fracture and adhesion properties [8–14], in lieu of modifications of materials in a chemical or physical way. Pillar and fibril interfaces are quite prevalent in natural structures, and these geometries have been shown to be integral to the superior mechanical properties, including enhanced toughness and strength, observed in many natural systems [15–18]. Some of the most widely investigated systems include gecko micro-fibril adhesives [19–24], mollusk byssus tendril adhesive structures [17], and human bone containing collagen fibrils [25]. In each of these systems, the existence of pillar/fibril structures are critical for improving toughness while maintaining strength.

From the early analysis by Griffith [26], it has been recognized that cracks and flaws give rise to stress concentrations and lead to failure via fracture at far field stresses that are well below the strength of the material. Analysis by Irwin [27] outlined the existence of a characteristic length scale, $\lambda_0 = \alpha \frac{E\mathcal{G}_c}{\sigma_y^2}$, where for ductile materials E is the Young's modulus, $\mathcal{G}_c$ is the fracture energy, σ_y is the yield strength, and α is a constant of order 1 that depends on the stress state and crack geometry (e.g., Irwin considered a penny-shaped crack, giving $\alpha = 1/\pi$). During fracture, the majority of the energy is dissipated over a zone of this length in front of a sharp crack [27]. A key challenge has been to find the right balance between the stiffness and resilience of materials, quantified through E and σ_y, and their toughness, quantified through $\mathcal{G}_c$. It is well-documented [28] that there is a trade-off between a material's intrinsic strength and its toughness, such that enhancement of one of these properties in a material through chemical or physical means typically results in a reduction in the other. In particular, methods to increase toughness of ductile materials by enlarging the process zone usually requires a decrease in the yield strength.

Many natural and engineered materials exhibit plasticity, which must be accounted for to fully understand and predict failure. In homogeneous materials, plasticity is one of the dominant mechanisms for obtaining high toughness; thus, plasticity may also be leveraged in architected materials to realize enhanced toughness. Yet, a fundamental understanding of the effects of plasticity and its role in toughening architected and structured materials remains lacking. Due to voids in a structured material, it can be difficult or inappropriate to apply fracture mechanics. Recent works on architected fracture [13,14], remain largely limited to linear elastic finite element simulations and analyses. A better understanding of architected plasticity will facilitate the design of materials with improved fracture resistance.

* Corresponding authors.
E-mail addresses: mibu@mpe.au.dk (M.K. Budzik), kturner@seas.upenn.edu (K.T. Turner).
[1] Present address: Engineering Systems, Inc., 10338 Miller Rd., Dallas, TX 75238

https://doi.org/10.1016/j.eml.2022.101912

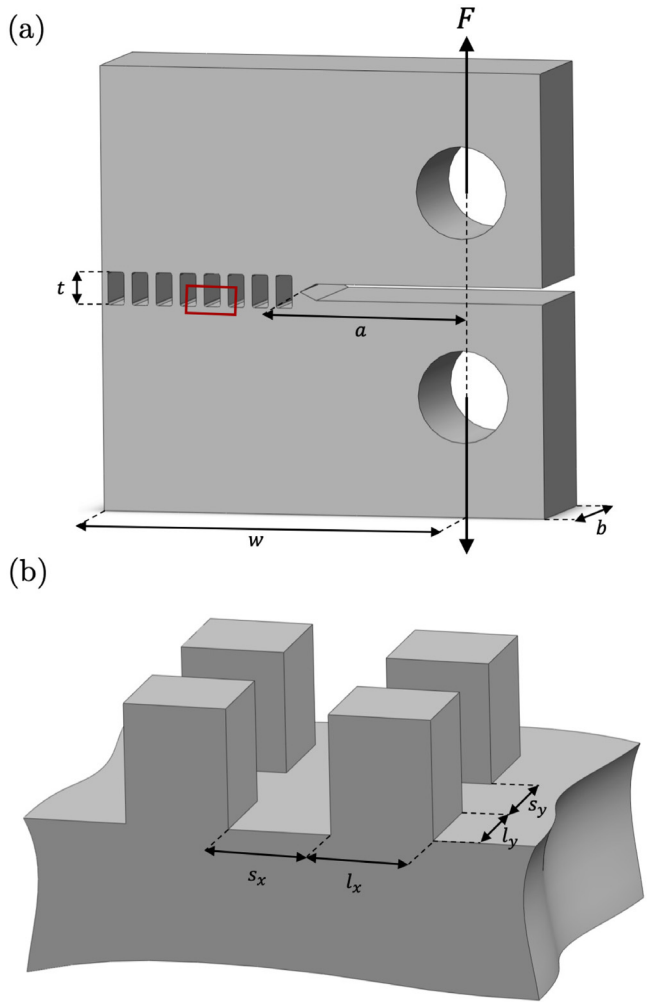

Fig. 1. (a) Compact tension specimen geometry; (b) Pillar fracture geometry corresponding to the region outlined in red in (a).

Using a simple pillar array as a model system, we demonstrate a route by which architecture can be used to control the extent of plasticity near a crack tip and, in turn, the effective toughness of a material. A pillar array was chosen since it is common in natural structures, and is also a geometry with relatively simple mechanics. Specifically, for pillars of sufficient height, we show that the process zone becomes isolated to the array. This is verified through experimental measurements of the process zone during fracture. Toughness measurements are presented for these experiments and show the significant effect architecture has on the effective toughness of the system. Utilizing the critical pillar height result, a relationship between the toughness is derived in terms of the process zone volume and the geometry of the array, which is verified from the experimental results. Finally, we discuss the toughness results in terms of the array's tensile strength and show that the two properties are decoupled in this system.

2. Effect of architecture on the process zone: Theory and experiments

We consider a compact tension (CT) geometry with a modified region near the fracture plane that contains a pillar array, as shown schematically in Fig. 1(a). Specifically, as shown in Fig. 1(b), an array with pillar dimensions l_x, l_y and t – or the lengths along x (along the crack path, a) and y (along the specimen depth, b), and the height, respectively – separated from each other by distances s_x and s_y, is examined. Thus, a representative area of the array, $A_t = (l_x + s_x)(l_y + s_y)$, will contain one pillar with area $A_l = l_x l_y$. With $s_y = 0$, the mechanics can be analyzed in 2-D.

During fracture, a plastic process zone of length λ_p will form ahead of the crack. The size of the process zone influences the toughness of the material, with a larger process zone typically dissipating more energy and increasing toughness. For a pillar array, the cross-sectional area of the pillars inside the process zone is $N_p A_l$, where N_p is the number of pillars within the zone. Along the process zone, there are n_x pillars along the crack path direction, a, such that $\lambda_p = \sum_i^{n_x}(l_x + s_x)_i$, and n_y pillars along the specimen depth, b, so that $b = \sum_i^{n_y}(l_y + s_y)_i$. Thus, the total number of pillars inside the process zone is $N_p = n_x n_y$, where n_x is determined by the process zone extension. An analysis of the CT specimen, modeled as two beams with a structured region in-between [13,29–31], which relates the process zone extension with the structural dimensions of the pillar array, l_i, s_i, and t, is provided in the Supplementary Material (SM), Section F. It has been shown previously [13] that, in the purely elastic case, the length over which high stresses are present near the crack tip (analogous to the process zone length) increases as a pillar array becomes more compliant because the stress at the crack tip is distributed across a greater number of pillars. Here, the same concept applies, but now a plastic process zone must be considered.

Pillar height, t, therefore, is a critical dimension as it affects the process zone dimensions both parallel and normal to the crack path. Increasing pillar height yields a more compliant array, and results in a longer plastic extension, λ_p, while each individual pillar also has a larger plastic volume. The analysis here is limited to cases where plasticity is confined to the pillar array, which is the case for pillars of sufficient height, as explained below.

Following Kanninen's approach [32], the stiffness of the beams in the cohesive region around the crack front can be expressed as $k^b = \mathcal{O}(Eb/\lambda_0)$, and the axial stiffness of the pillars at the crack front is $k^p = \mathcal{O}\left(E(n_y l_y)/t\right)$. The $\mathcal{O}$ symbol is used to denote that the stress state may potentially vary along b. The overall stiffness of the cohesive zone in the vicinity of the crack tip, k, can then be found by considering these regions in series, such that $k^{-1} = k^{p^{-1}} + k^{b^{-1}}$. This implies that whichever region is more compliant will contribute more to the effective behavior. As $t \to 0$, the stiffness of the array is infinite and the compliance of the beam will control the behavior. As pillar height increases, the array will become more compliant than the beams (i.e., $k^p \leq k^b$). Comparing the two expressions above, a critical pillar height is obtained, $t_c = \mathcal{O}\left(\lambda_0 \frac{l_y n_y}{b}\right)$. If $t > t_c$, the pillar array becomes more compliant than the beams and the deformation in the system will begin to localize to the array. Assuming that dimensions s_y, $l_y \ll b$, the stress can be considered as constant through the depth, and substituting in for b and n_y results in

$$t_c \approx \lambda_0 \frac{l_y}{l_y + s_y}. \tag{1}$$

For a planar (2D) geometry (i.e. $s_y = 0$), Eq. (1) predicts $t_c \approx \lambda_0$. This is indeed the only length scale associated with the problem, as outlined in Irwin [27]. In any other case, choosing a pillar height significantly above t_c allows the plastic deformation to be fully confined to the pillar region.

For the case of $t < t_c$, two scenarios are possible: the one already discussed, for which $t \to 0$, and an intermediate height

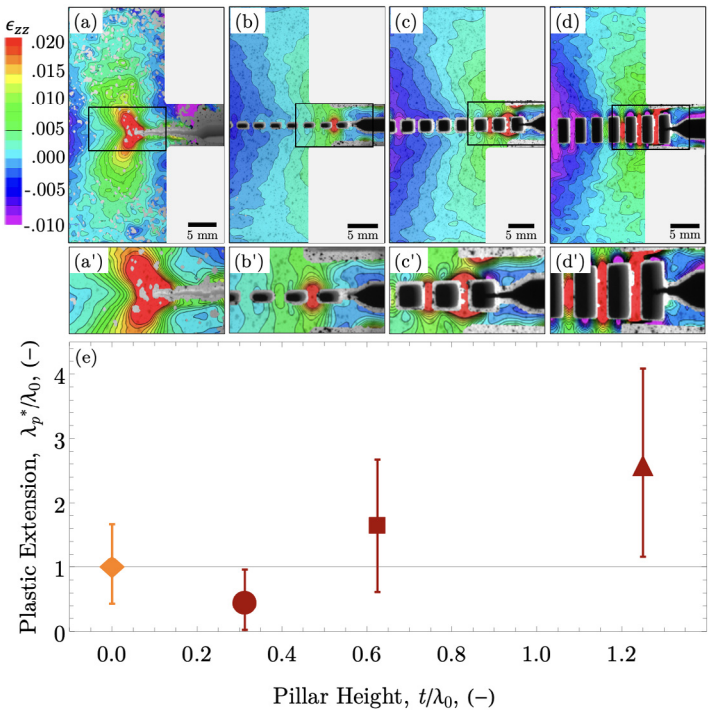

Fig. 2. Normal strain near the crack tip measured via DIC for (a) a homogeneous specimen, (b) a specimen with $l_x = 1,\ s_x = 2,\ s_y = 0,\ t = 1$ mm, (c) the same array with $t = 2$ mm, and (d) the same array with $t = 4$ mm. Blank regions correspond to areas of the specimens obscured by experimental setup. (a′–d′) Plastic regions for the four geometries shown, corresponding to the framed regions of top-row of sub-figures. (e) Relative plastic extension for relative pillar height. Standard errors for the measurements are shown.

$0 < t < t_c$. The latter requires plasticity in both the bulk and pillar portions to be recognized as energy dissipation sources. Thus, the different features of the interface geometry, i.e. l_y, s_y, are likely to control the stress transfer between the solid and the pillar regions. In addition, the aspect ratios, t/l_i, and the density of pillars, A_l/A_t, can be selected to control the process zone extension and the overall plastic volume. These two cases are out of the scope of this work, and we will restrict our analyses to the case of $t > t_c$, where plasticity is assumed to be isolated to the pillar array.

To verify the prediction of a critical pillar height, and to evaluate the effect of pillar geometry on toughness, polyamide 12 (PA 12, Nylon) CT specimens, additively manufactured via selective laser sintering (SLS), were tested as a model system under quasistatic loading conditions (details in Section 6). Force–displacement data was recorded and strain near the crack tip was measured using imaging and digital image correlation (DIC). Additional details on DIC measurements can be found in the SM, Section D. Fig. 2 shows measured strains for four different specimen geometries. These measurements show the localization of the plasticity in the pillars, and the increase in process zone length as pillar height increases.

Fig. 2(a–d), and the corresponding magnified versions (a′–d′), show the gradual transition in the strain field (ϵ_{zz} is the component in the loading direction) as t increases from $t = 0$ to $t > t_c$. These strain measurements were acquired during steady-state crack growth for the reference specimen, Fig. 2(a), and immediately before the peak fracture loads for Fig. 2(b–d), such that the plastic regions are all fully-formed for each specimen. The maximum value on the strain scale is the yield strain measured via tensile testing (see SM, Section B). In the reference specimen, the strain is localized near the crack tip (Fig. 2(a)). For this material, the estimated plastic radius from the Irwin model [27] given above is $\lambda_0 = 3.2 \pm 0.7$ mm, assuming plane-stress conditions—this is consistent with the size of the plastic zone observed in Fig. 2(a), which is 3.5 ± 0.5 mm. Note that plane stress conditions are used here, as DIC measures the strain on the surface, despite the overall specimen being under plane strain. As the height of the pillars increases (Fig. 2(b)), i.e. $t \gtrsim 0$, the combined effect of a relatively sharp crack and a discrete geometry results in the localization of the peak strain in the pillar region, however, over relatively small volume. In Fig. 2(c), both the pillar region and a part of the bulk specimen are affected; however, the pillars appear to contribute more to the plastic dissipation as t approaches t_c. In Fig. 2, $s_y = 0$, thus $t_c \approx \lambda_0 = 3.2$ mm. In Fig. 2(d), the plastic region is fully contained within the pillar regions and the plastic deformation in the beams is negligible, i.e. $t > t_c$. Fig. 2(e) shows the DIC-measured extension of the plastic zone λ_p^* as a function of pillar height, t, with both axes normalized by λ_0. We note the gradual increase of the plastic zone extension as the pillar height is increased (for the same area fraction, A_l/A_t).

3. Toughness of architected interfaces: Theory and experiments

The CT specimens were tested (see Section 6 for details) and the toughness [27,33], J^*, was calculated as

$$J^* = \frac{K_{IC}^2}{\bar{E}} \propto F_{max}^2, \tag{2}$$

where $\bar{E} = \frac{E}{1-\nu^2}$, ν is the Poisson's ratio, and K_{IC} is the critical stress intensity factor [34], which is proportional to the failure load of the specimen, F_{max}. Due to the architected region in the vicinity of the crack, J^* is the "effective toughness", and

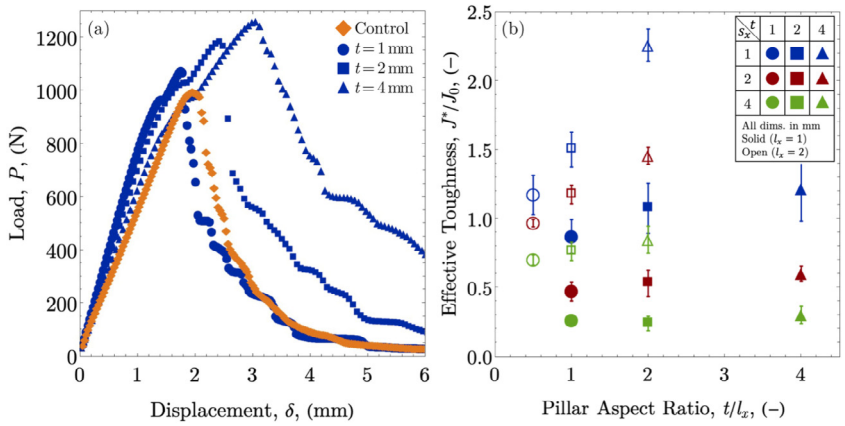

Fig. 3. (a) Representative load–displacement curves for a reference specimen and three architected specimens. (b) Effective toughness of pillar specimens, J^*, relative to the toughness of a homogeneous specimen, J_0, for the given pillar aspect ratio, t/l_x. For both plots, blue, red, and green markers denote arrays with $s_y = 0$ and $s_x = 1, 2, 4$ mm, respectively. Orange markers denote the reference specimen. Closed versus open markers denote $l_i = 1, 2$ mm, respectively. (For interpretation of the references to color in this figure legend, the reader is referred to the web version of this article.)

is no longer an intrinsic material property. K_{IC} was calculated from the experimentally measured F_{max}, as detailed in the SM, Section E. Reference CT specimens (of the same dimensions and geometry, but without pillars) were also fabricated and tested. For the reference specimens, the intrinsic toughness of the material is measured, J_0, as small scale yielding conditions were met. Throughout this work, the effective toughness of the architected specimens will be considered relative to the reference value.

Representative load–displacement curves for the reference and three architected specimens are shown in Fig. 3(a), and show linear behavior up to a critical load, when a precracked ligament that is before the first pillar is fractured. The peak load for all the architected specimens was observed to occur as the first pillar fails. As the features of the arrays are small compared to the plastic radius ($s_x < \lambda_0$, $l_x < \lambda_0$), the load–displacement curves resemble that of the reference specimen, with a clear peak load and relatively smooth damage curve.

The effective toughness values of pillar arrays with $s_y = 0$ are given in Fig. 3(b) as a function of the pillar aspect ratio, t/l_x. The full set of experimental results may be found in the SM, Table S1. Toughness can be tuned over a significant range, from ∼25% to >200%, relative to the reference specimen. For a given pillar width and spacing, toughness is enhanced by increasing pillar height (Fig. 3). In the elastic case [13] for planar pillar geometries, aspect ratio controlled the effective toughness of the array. In the case of elastic–plastic failure shown here, pillar aspect ratio does not account for all variation in toughness, as distinct magnitudes and trends are apparent for specimens with varying pillar widths and spacings. A new analysis, which considers the effects of plastic dissipation in pillar fracture, is required to understand and predict the toughness.

We provide an energy analysis of the system, restricted to the case of geometries where $t \gtrsim t_c$, and all other structural dimensions, l_i, $s_i \leq \mathcal{O}(\lambda_0)$. As a result, the plastic zone is assumed to be fully confined to the pillar region, simplifying the analysis. We consider the general potential energy function, Π,

$$\Pi = \int_V U_e dV + \int_V U_p dV + \int_\Gamma \gamma_s dA - \int_V b_i u_i dV - \int_{\partial V} t_i u_i dA \quad (3)$$

where U_e is the elastic strain energy density, U_p is the plastic energy density, γ_s is the surface energy, and $\int_V b_i u_i dV + \int_{\partial V} t_i u_i dA$ is the work done by external forces, body and surface, respectively, where V corresponds to volume, Γ to the crack area, and ∂V refers to the boundary area of V. The plastic energy $U_p = \int_\epsilon K\epsilon^m d\epsilon$, where K is the plastic modulus and m is the hardening exponent, which are both material constants. For the case considered here, with only pillar plasticity, we can write:

$$\int_V U_p dV \approx t N_p (l_x l_y) \int_\epsilon K\epsilon^m d\epsilon. \quad (4)$$

Eq. (4) dictates that, for plastic dissipation-dominated geometries, the resulting fracture properties depend mainly on the number of pillars inside the plastic process zone, as well as the base material properties expressed through K and m. In addition, as detailed in the SM, Section F, the length of the plastic process zone λ_p, and therefore the value of N_p, is an implicit function of t, s_i, and l_i, which makes manipulating local geometry a powerful tool to tune the toughness. Considering the first variation of Eq. (3) and setting equal to zero (i.e., $\delta\Pi = \frac{\partial \Pi}{\partial A}\delta A = 0$), provides the condition for crack propagation to occur, specifically:

$$\frac{\partial}{\partial A}\left(\int_V U_e dV + \int_V U_p dV\right) + \Gamma_0 - \int_\Delta P d\delta = 0, \quad (5)$$

where $\int_\Delta P d\delta = \frac{\partial}{\partial A}\left(\int_V b_i u_i dV + \int_{\partial V} t_i u_i dA\right)$, and $\Gamma_0 = \frac{\partial}{\partial A}\int_\Gamma \gamma_s dA$ is the toughness in the absence of plasticity. Rearranging terms leads to a familiar form of the condition,

$$\int_\Delta P d\delta - \frac{\partial}{\partial A}\left(\int_V U_e^b dV\right) = \frac{\partial}{\partial A}\left(\int_V U_p^p dV\right) + \Gamma_0 \equiv J_c, \quad (6)$$

where the left-hand side of the equation corresponds to the energy release rate [35], and the right-hand side is the energy per unit crack area required for crack advance, here denoted as J_c, which is the effective fracture toughness of the system. For the case where plasticity is isolated to the pillar array, the following relation can be obtained by substituting Eq. (4) into the expression for J_c, resulting in

$$J_c = t N_p (l_x l_y)\left[\frac{\partial}{\partial A}\int_\epsilon K\epsilon^m d\epsilon\right] + \Gamma_0, \quad (7)$$

which connects the energy required to propagate the crack with the characteristic dimensions of the pillar array. If plasticity is the dominant form of energy dissipation, changes in the surface energy term for varying geometries will be comparatively small and can be neglected, so its relative contribution is taken as a constant. Thus, comparing to the toughness of a homogeneous

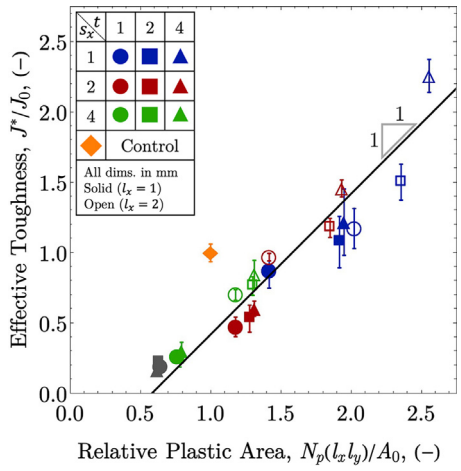

Fig. 4. Effective toughness of pillar specimens, J^*, relative to the toughness of a homogeneous specimen, J_0, for the given specimen plastic zone area, $N_p(l_x l_y)$, relative to the plastic zone area of a homogeneous specimen, A_0. Blue, red, and green markers denote arrays with $s_y = 0$ and $s_x = 1, 2, 4$ mm, respectively, while gray markers denote arrays with $s_x = s_y = 1$ mm. Closed versus open markers denote $l_i = 1, 2$ mm, respectively. (For interpretation of the references to color in this figure legend, the reader is referred to the web version of this article.)

specimen, J_0, the relative toughness is

$$\frac{J_c}{J_0} = \beta \frac{t N_p (l_x l_y)}{V_0} + \frac{\Gamma_0}{J_0}, \tag{8}$$

where V_0 is the plastic volume of the homogeneous specimen, and β is the quotient of the derivatives of the pillar and homogeneous plastic integrals. Thus, we find a linear relationship between J_c/J_0 and $tN_p(l_x l_y)/V_0$, with slope β, where N_p depends on the critical dimensions of the pillar array, l_i, s_i, and t. Since the plastic dissipation for a given volume of material is identical for homogeneous and architected specimens, their per-unit volume plastic integrals will be equal, leading to $\beta = 1$.

Fig. 4 again shows the effective toughness, normalized by the toughness of the reference configuration, J^*/J_0, but now as a function of the plastic area in the pillar region, relative to the plastic area of a homogeneous specimen. In this figure the plastic areas are calculated from the plastic extensions, λ_p, found using the Timoshenko beam theory analysis in the SM, Section F. As expected from the energy analysis, a linear scaling is observed, and a linear fit with fixed $\beta = 1$ results in $\frac{\Gamma_0}{J_0} = -0.58$ (with $R^2 = 0.97$). These results suggest that the measured effective toughness scales with the plastic area rather than volume, as predicted by Eq. (8). Calculating J^* using Eq. (2) has consequences that can be observed by comparing Eqs. (2) and (7). Critically, J^* considers the modulus of the bulk specimen expressed as $\bar{E}$, while for an architected specimen, the effective modulus is equally controlled via the local architecture, and is proportional to t, consistent with Eq. (6) and [32].

4. Geometrically decoupling toughness and strength

It is apparent from the results in Figs. 2–4, that increasing pillar height can result in longer plastic extension and thus a larger effective toughness, without the need to modify the area fraction, A_l/A_t, through changes in pillar width or spacing. This is useful because only the area fraction, and not the pillar height, controls the effective tensile strength of the pillar array. Given a material with intrinsic tensile strength, σ_{f_0}, the relative effective strength of the pillar array, σ_f^*, under uniform tension is

$$\frac{\sigma_f^*}{\sigma_{f_0}} = \frac{A_l}{A_t} = \frac{l_x}{l_x + s_x}\frac{l_y}{l_y + s_y}. \tag{9}$$

This result was verified experimentally for our case, using SLS PA 12 pillar tensile specimens, with the results shown in Fig. 5(a). Results are plotted over the measured area fraction of each specimen with the point at (1, 1) corresponding to a standard tensile measurement of a homogeneous specimen, with all pillar array specimens necessarily having lower tensile strength due to introduced void spaces.

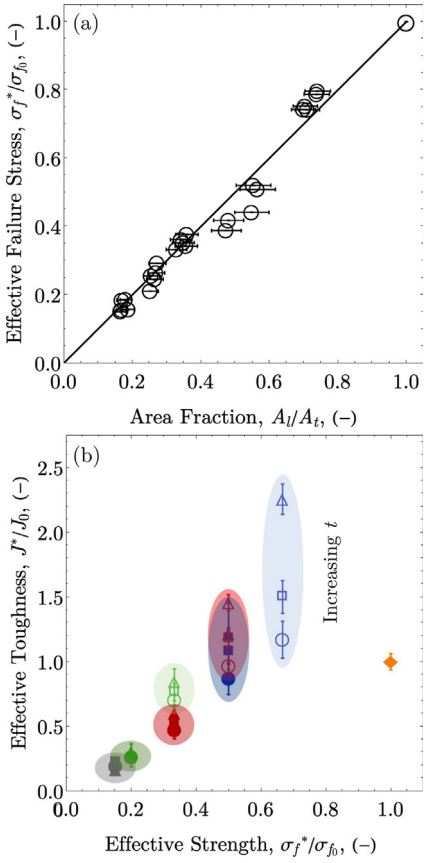

Fig. 5. (a) Tensile strength results for varying area fractions, compared to the theoretical value from Eq. (9) using the specimen's measured area fraction (value ± std. error); (b) Effective toughness of pillar specimens, J^*, relative to the toughness of a homogeneous specimen, J_0, for a given strength, relative to a homogeneous specimen. Blue, red, and green markers denote arrays with $s_y = 0$ and $s_x = 1, 2, 4$ mm, respectively, while gray markers denote a arrays with $s_x = s_y = 1$ mm. Closed versus open markers denote $l_i = 1, 2$ mm, respectively. (For interpretation of the references to color in this figure legend, the reader is referred to the web version of this article.)

However, we observe that, for a pillar array with a given tensile strength, the effective toughness can be enhanced by varying pillar height without any additional loss in effective tensile strength. From a design standpoint, Fig. 5(b) outlines the effective toughness as a function of the effective tensile strength, calculated through Eq. (9). The tensile strength is proportional to the total cross-sectional area of the pillar array, and is independent of pillar height; but, for a given pillar distribution and resulting strength, toughness can be tuned independently by varying pillar height. Thus, strength and toughness are decoupled through the use of architecture, which enables improvements in toughness without loss of strength. Furthermore, these results suggest that high aspect-ratio (i.e. very tall), clustered pillar arrays, will be the

design that maximizes toughness with minimal loss of strength. Within the configurations evaluated in this work, geometry was used to increase toughness by more than 2× relative to the bulk material, with only a 33% loss in strength. At that given strength, varying pillar height allowed for tuning the toughness from being approximately equal to the intrinsic value to more than 2× greater. The only limitations to improving the toughness for a given strength arise from size constraints on the specimen, which would eventually limit the size of the plastic extension, or practical limitations arising from a particular material/fabrication process that constrains the feasible pillar geometries.

5. Conclusions

We have shown that there is a critical height for pillar arrays, above which plasticity is confined to the pillar region and a simple linear relationship exists between the toughness and the plastic pillar area. Furthermore, toughness increases with pillar height due to greater plastic extension. This enhancement in toughness is achieved without loss in relative strength at a particular area fraction. Thus, geometry provides a route to decouple strength from toughness, and indicates that architecture is an important material design parameter. The effect of geometry found here should be fully transferable to other materials, as long as the geometry is appropriately tailored in conjunction with the material's intrinsic properties and length scale, λ_0. Finally, while a simple pillar array was chosen for this work to illustrate the method, the approaches applied here can be similarly applied to other architected materials, with the appropriate micromechanics applied for the particular geometry.

6. Materials and methods

Compact tension specimens were fabricated via 3-D selective laser sintering (SLS) of polyamide 12 [36–39], specifically DuraForm® ProX Polyamide (PA) 12 (3D Systems® Inc, USA), which is optimized for printing via SLS and has a median particle diameter of ∼50 μm [40]. Specimens were fabricated using a 3D Systems® ProX™ 500 SLS 3D Production Printer, using a blend of 50% virgin and 50% recycled powder, and a laser power of 2.6 J/cm^2. Specimens were cleaned manually and by using a grit blaster with superfine alumina media, as recommended by the manufacturer. Tensile properties were measured and are detailed in the SM, Section B.

SLS PA 12 was chosen due to its relatively low anisotropy compared to many other additive manufacturing approaches, and its ability to print specimens with fine scale architecture [37,38,40]. In SLS printing, specimens are fabricated by locally sintering successive layers of material. Each additional layer bonds to the previous one during sintering and increases the specimen depth. The fracture toughness is essentially invariant for cracks with surfaces orthogonal to the print plane, but has been shown to be ∼10%–15% lower for cracks parallel to the print plane (i.e., cracks that propagate between individual print layers) [38]. For this work, specimens were printed so all crack planes were orthogonal to the print plane.

The compact tension specimens [34,41], as shown in Fig. 1(a) were fabricated with width $w = 45$ mm, depth $b = 15$ mm, and a printed precrack length $a = 22$ mm, ($a/w \approx 0.49$, which is within the proper bounds [41]). A small solid ligament was printed in front of the first rectangular void space, to help ensure the crack onset along the symmetry plane of the specimen. All pillar junctions had a fillet with a radius $r = 0.2$ mm to reduce any effects from stress concentrations. The specimens were tested in an MTS Criterion Model 43 (MTS Systems Corporation, USA) fitted with pin-mounted grips. Fracture experiments were performed under displacement control at a constant rate of 2 mm/min, which resulted in stable crack propagation and quasistatic conditions. Load–displacement measurements were corrected for machine compliance. Specimens were precracked with a razor, but the critical stress intensity factor was calculated when the first pillar failed, which corresponded, in all cases, to the maximum load the specimen achieved. Five specimens of each geometry were tested. There was good reproducibility, as indicated by the low standard deviations in the results shown in Figs. 3–4. Details regarding calculation of the critical stress intensity factor can be found in the SM, Section E.

Before fracture testing, at least one specimen for each of the pillar array configurations was coated with a speckle pattern using black paint applied with an airbrush to enable digital image correlation (DIC) of the side face. A single DIC specimen per geometry was deemed sufficient due to the very good reproducibility of the fracture testing results, as well as because of the numerous configurations tested. During fracture testing, images were acquired using a Guppy Pro F-201 camera (Allied Vision, Germany) at 14 Hz rate (the camera and the testing machine were synchronized). The recordings were processed using the DIC software Vic2D (version 6, Correlated Solutions, USA) two-dimensional (2D) to track the displacement field. After removing rigid body motions, the displacement field and its derivatives (i.e. strain and rotations) were extracted and post-processed in the open-source image analysis software ImageJ to evaluate the plastic volume size, as shown in Fig. 2. Additional details regarding the DIC analysis can be found in the SM, Section D.

For strength testing of pillar arrays, custom pillar tensile specimens were fabricated using a 3D Systems® sPro140™ SLS printer, with width $w = 24$ mm, depth $b = 3.2$ mm, and nominal pillar area fractions $\frac{A_l}{A_t} = \frac{1}{6}, \frac{1}{3}, \frac{1}{4}, \frac{1}{2}$, and $\frac{2}{3}$. Pillars had dimensions $t = 1$ mm and $l_x = 1$ ($l_x = 2$ mm for the case of $\frac{A_l}{A_t} = \frac{2}{3}$), and additional specimens were fabricated for the case of $\frac{A_l}{A_t} = \frac{1}{2}$ with $t = 2$ and 4 mm to verify that the strength is independent of pillar height. All pillar junctions had a fillet radius $r = 0.2$ mm. Specimens were tested using the same grips as the CT specimens, under displacement control at a rate of 1 mm/min, which roughly matched the time to failure of the CT specimens. All specimens failed in an unstable manner, with the peak load, $F = F_{max}$ used to calculate the failure stress. An effective failure stress is considered, $\sigma_f^* = \frac{F_{max}}{wb}$, with the results normalized by the intrinsic failure stress of the material, σ_{f_0}. Five specimens for each geometry were tested. An image of a representative pillar tensile specimen is given in Fig. S1, and the results for varying pillar height are given in the SM, Section C.

Declaration of competing interest

The authors declare that they have no known competing financial interests or personal relationships that could have appeared to influence the work reported in this paper.

Data availability

Data will be made available on request.

Acknowledgments

This research was funded primarily by the National Science Foundation (NSF) MRSEC program under award DMR-1720530. MKB would like to thank Aarhus University Research Foundation (AUFF) (grant number 28653). SF acknowledges support from the Department of Defense (DoD) through the National Defense Science & Engineering Graduate (NDSEG) Fellowship Program.

Appendix A. Supplementary data

Supplementary material related to this article can be found online at https://doi.org/10.1016/j.eml.2022.101912.

References

[1] T. Schaedler, A.J. Jacobsen, A. Torrents, A.E. Sorensenm, J. Lian, J. Greer, L. Valdevit, W. Carter, Ultralight metallic microlattices, Science 334 (6058) (2011) 962–965.

[2] L.R. Meza, S. Das, J.R. Greer, Strong, lightweight, and recoverable three-dimensional ceramic nanolattices, Science 345 (6202) (2014) 1322–1326.

[3] X. Zheng, H. Lee, T.W. Weisgraber, M. Shusteff, J. Dotte, E. Duoss, J.D. Kuntz, M. Biener, Q. Ge, J. Jackson, S. Kucheyev, N. Fang, C.M. Spadaccini, Ultralight, ultrastiff mechanical metamaterials, Science 344 (6190) (2014) 1373–1326.

[4] R. Ramachandramoorthy, M. Mieszala, C.V. Manzano, X. Maeder, J. Michler, L. Philippe, Dual-templated electrodeposition and characterization of regular metallic foam based microarchitectures, Appl. Mater. Today 20 (2020) 100667.

[5] M.F. Ashby, The properties of foams and lattices, Philos. Trans. R. Soc. A 364 (2005) 15–30.

[6] M. Pham, C. Liu, I. Todd, J. Lertthanasarn, Damage-tolerant architected materials inspired by crystal microstructure, Nature 565 (2019) 305–313.

[7] M.M. Abedi, R.J. Nedoushan, W. Yu, Enhanced compressive energy absoprtion properties of braided lattice and polyurethane foam hybrid composites, Int. J. Mech. Sci. 207 (2021) 1–16.

[8] S. Xia, L. Ponson, G. Ravichandran, K. Bhattacharya, Toughening and asymmetry in peeling of heterogeneous adhesives, Phys. Rev. Lett. 108 (2012) 817–822.

[9] N. Brodnik, S. Brach, C. Long, G. Ravichandran, B. Bourdin, K.T. Faber, K. Bhattacharya, Fracture diodes: Directional asymmetry of fracture toughness, Phys. Rev. Lett. 126 (2021).

[10] L. Zhang, X. Mao, Fracturing of topological Maxwell lattices, New J. Phys. 20 (2018) 1–11.

[11] X. Mao, T.C. Lubensky, Maxwell lattices and topological mechanics, Annu. Rev. Condens. Matter Phys. (2018) 413–433.

[12] A.J. Mateos, W. Huang, Y. Zhang, J.R. Greer, Discrete-continuum duality of architected materials: Failure, flaws, and fracture, Adv. Funct. Mater. 29 (2019) 1–7.

[13] S. Heide-Jorgensen, M.K. Budzik, K.T. Turner, Mechanics and fracture of structured pillar interfaces, J. Mech. Phys. Solids 137 (2020) 1–20.

[14] A.J.D. Shaikeea, H. Cui, M. O'Masta, X.R. Zheng, V.S. Deshpande, The toughness of mechanical metamaterials, Nature Mater. (2022).

[15] J.Y. Chung, M.K. Chaudhury, Roles of discontinuities in bio-inspired adhesive pads, J. R. Soc. Interface 2 (2005) 55–61.

[16] N.J. Glassmaker, A. Jagota, C.-Y. Hui, W.L. Noderer, M.K. Chaudhury, Biologically inspired crack trapping for enhanced adhesion, Proc. Natl. Acad. Sci. USA 104 (26) (2007) 10786–10791.

[17] F. Barthelat, Z. Yin, M.J. Buehler, Structure and mechanics of interfaces in biological materials, Nat. Rev. Mater. 1 (2016) 1–16.

[18] M. Bacca, J.A. Booth, K.L. Turner, R.M. McMeeking, Load sharing in bioinspired fibrillar adhesives with backing layer interactions and interfacial misalignment, J. Mech. Phys. Solids 96 (2016) 428–444.

[19] N. Glassmaker, A. Jagota, C.-Y. Hui, J. Kim, Design of biomimetic fibrillar interfaces: 1. Making contact, J. R. Soc. Interface 1 (2004).

[20] C.-Y. Hui, N. Glassmaker, T. Tang, A. Jagota, Design of biomimetic fibrillar interfaces: 2. Mechanics of enhanced adhesion, J. R. Soc. Interface 1 (2004).

[21] B. Aksak, M.P. Murphy, M. Sitti, Gecko inspired micro-fibrillar adhesives for wall climbing robots on micro/nanoscale rough surfaces, in: IEEE International Conference on Robotics and Automation, 2008.

[22] K. Autumn, N. Gravish, Gecko adhesion: evolutionary nanotechnology, Philos. Trans. R. Soc. A 366 (2008) 1575–1590.

[23] M.D. Barlett, A.B. Croll, D.R. King, B.M. Paret, D.J. Irschick, A.J. Crosby, Looking beyond fibrillar features to scale gecko-like adhesion, Adv. Mater. 24 (2012) 1078–1083.

[24] A.K. Geim, S.V. Dubonos, I. Grigorieva, K. Novoselov, A. Zhukov, S.Y. Shapoval, Microfabricated adhesive mimicking gecko foot-hair, Nature Mater. 2 (2003) 461–463.

[25] Q. Yang, B.N. Cox, R.K. Nalla, R. Ritchie, Fracture length scales in human cortical bone: the necessity of nonlinear fracture models, Biomaterials 27 (2006) 2095–2113.

[26] A.A. Griffith, VI. The phenomena of rupture and flow in solids, Philos. Trans. R. Soc. Lond. Ser. A 221 (582–593) (1921) 163–198.

[27] G.R. Irwin, Analysis of stresses and strains near the end of a crack transversing a plate, Trans. ASME Ser. E J. Appl. Mech. 24 (1957) 361–364.

[28] R.O. Ritchie, The conflicts between strength and toughness, Nature Mater. 10 (2011) 817–822.

[29] D.A. Dillard, B. Mukherjee, P. Karnal, R.C. Batra, J. Frechette, A review of Winkler's foundation and its profound influence on adhesion and soft matter applications, Soft Matter 14 (2018) 3669–3683.

[30] C. Chow, T. Liu, C. Woo, Fracture toughness determination for compact tension specimens, Theor. Appl. Fract. Mech. 4 (1985).

[31] X. Chen, T. Yu, Elastic-plastic beam-on-foundation under quasi-static loading, Int. J. Mech. Sci. 42 (2000).

[32] M. Kanninen, An augmented double cantilever beam model for studying crack propagation and arrest, Int. J. Fract. 9 (1) (1973) 83–92.

[33] J.R. Rice, Conserved integrals and energetic forces, in: Fundamentals of Deformation and Fracture, Cambridge University Press, Cambridge, 1985, pp. 33–56.

[34] ASTM, E399-20a: Standard Test Method for Linear-Elastic Plane Strain Fracture Toughness of Metallic Materials, ASTM, 2020.

[35] J. Lubliner, Plasticity Theory, Macmillan Publishing Co., 1990.

[36] R. Goodridge, C. Tuck, R. Hague, Laser sintering of polyamides and other polymers, Prog. Mater. Sci. 57 (2012) 229–267.

[37] A. Cano, A. Salazar, J. Rodriguez, Effect of temperature on the fracture behavior of polyamide 12 and glass-filled polyamide 12 processed by selective laser sintering, Eng. Fract. Mech. (2008).

[38] T. Brugo, R. Palazzetti, S. Ciric-Kostic, X. Yan, G. Minak, A. Zucchelli, Fracture mechanics of laser sintered cracked polyamide for a new method to induce cracks by additive manufacturing, Polym. Test. 50 (2016) 301–308.

[39] B. Caulfield, P. McHugh, S. Lohfeld, Dependence of mechanical properties of polyamide components on build parameters in the SLS process, J. Mater Process. Technol. 182 (2007) 477–488.

[40] E.D. Bain, E.J. Garboczi, J.E. Seppala, T.C. Parker, K.B. Migler, AMB2018-04: Benchmark physical property measurements for powder bed fusion additive manufacturing of polyamide 12, Integr. Mater. Manuf. Innov. (2019).

[41] ASTM International, ASTM D5045-99: Standard Test Methods for Plane-Strain Fracture Toughness and Strain Energy Release Rate of Plastic Materials, ASTM International, West Conshohocken, PA, USA, 2007.